sciendo

LATVIAN JOURNAL OF PHYSICS
AND TECHNICAL SCIENCES
2024, N 4

DOI: 10.2478/lpts-2024-0026

# INVESTIGATION OF CENOSPHERE-BASED LIGHTWEIGHT CERAMIC MATRIXLESS SYNTACTIC FOAM THROUGH SPARK PLASMA SINTERING

T.V. Eiduks, R. Drunka, V. Abramovskis, I. Zalite,
P. Gavrilovs, J. Baronins, V. Lapkovskis

Faculty of Natural Sciences and Technology,
Riga Technical University
3 Paula Valdena Str., Riga, LV-1048, LATVIA
*e-mail: vjaceslavs.lapkovskis@rtu.lv

The current study introduces porous ceramic materials fabricated from cenospheres through spark plasma sintering. The investigation delves into the impact of sintering temperature, mould diameter (20 and 30 mm), and cenosphere size on the resulting material properties. Notably, sample shrinkage initiates at 900 °C and demonstrates an upward trend with temperature escalation, while a larger mould diameter contributes to sample shrinkage. Elevated sintering temperature leads to increased apparent density across various sample series, such as CS 63–150 μm in a 20 mm mould (0.97 to 2.3 g/cm³ at 1050–1300 °C), CS 150–250 μm in a 20 mm mould (0.93 to 1.96 g/cm³ at 1050–1200 °C), and others in different mould sizes. Total porosity decreases from 61.5 % to 3.9 % with a rising sintering temperature (1050 to 1250 °C), while open porosity starts decreasing at lower temperatures. Closed porosity peaks in samples sintered at 1150 °C. Furthermore, an increase in sintering temperature from 1050 to 1300 °C boosts the compressive strength of CS 63–150 samples in a 20 mm mould from 11 MPa to 312 MPa. These findings align with the Rice model, illustrating an exponential relationship between compressive strength, material porosity, and fully dense material compressive strength.

***Keywords:*** *Cenospheres, porosity, porous ceramics, shrinkage, spark plasma sintering.*

## 1. INTRODUCTION

In the contemporary industrial landscape, there is a pressing need to innovate and produce lightweight and durable materials. This dual objective allows for creating more structurally efficient objects, necessitating reduced material usage and enabling compact designs, thus leading to economic benefits. In the context of vehicles, these benefits bring about energy conservation during their operation.

When developing a composite material, it becomes feasible to combine the distinctive properties of various materials into one [1]. To guarantee a high level of strength in the composite, it is important to incorporate a material inherently to have high strength [2], [3]. One of the promising components of lightweight materials is cenospheres (CS). These cenospheres are derived from the residue generated by coal-burning thermal power plants. A substantial quantity of ash, comprising cenospheres, is formed during coal combustion. The separation of cenospheres from the ash contributes to a reduction in waste produced by thermal power stations. It offers an opportunity to harness these unique ceramic particles for composite material development.

Cenospheres, derived from coal combustion residues, are available at a low cost as a component of fly ash from coal-fired power plants. They are characterised as chemically inert [4] and resistant to high temperatures, making them a successful type of hollow ceramic microbead for use as filler particles. These cenospheres have proven suitability, even with high-temperature processes [5]. The apparent density of cenospheres ranges from 0.4 to 0.8 g/cm$^3$, although depending on the definition, i.e. whether cenospheres are described as particles with an apparent density below that of water or as hollow particles, the maximum density will approach that of an alloy, i.e., about 2–2.6 g/cm$^3$ [6]. This happens because gas bubble is trapped in the centre of the particles, despite higher density of the material forming the cenosphere, which has a composition similar to that of flue gases, and also due to the fact that for different particle sizes, the ratio of diameter to wall thickness is constant at around 20–30 [7]. The diameter of the cenospheres ranges from 5 μm to over 600 μm, although most of the particles are between 20 μm and 300 μm in diameter [8].

Employing the CS, it is possible to synthesise lightweight composites called syntactic foams (SF) with enhanced mechanical properties and reduced weight [9]. SF synthesis typically uses matrix materials that are combined hollow spherical spheres (or microspheres) like glass hollow microbaloons [10], ceramic hollow spheres [11]–[13] or CS. Past decade CS was actively studied for a new SF design [14], [15], using various matrices: polymer [16]–[18], ceramic [19], [20], glass [21], [22], metals [23]–[25], natural ceramics (clay) [26], [27], cement [28], [29], hybrid materials [30], [31] and natural source matrix [10], [32]. However, a new version of SF, a matrix-less SF, was introduced. In this approach, CS was coated by metal using physical vapour deposition [33] and sintered by spark plasma sintering (SPS) to obtain single-piece material [34].

Spark plasma sintering stands out for its ability to control microstructure and adapt heating parameters through pulsed direct current and pressure. In the case of conductive materials, the formation of inter-particle contacts includes local melting. When employed as a furnace, SPS facilitates

high-rate heating for pre-consolidated specimens. Additionally, the utilisation of space holders in SPS allows for precise control over the structure of pore walls. Like other sintering techniques, SPS enables the creation of porous materials through methods such as partial densification, sintering hollow or porous particles, utilising decomposing pore formers, or employing space holders that are extracted during post-sintering (Fig. 1) [35].

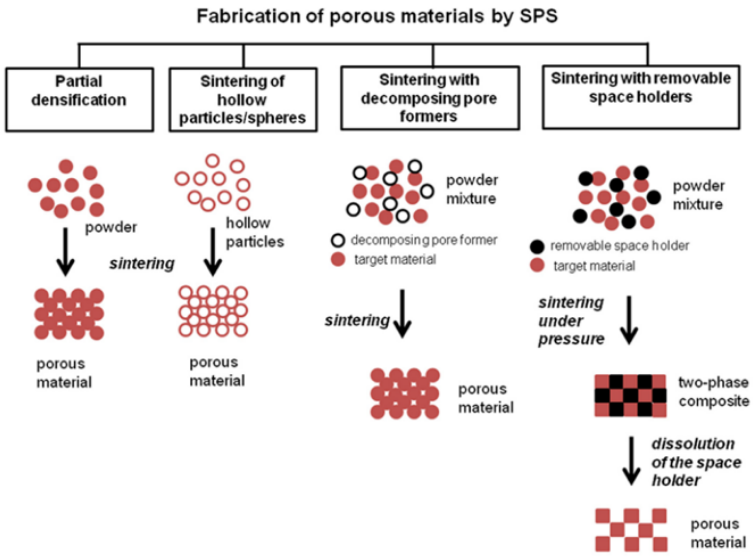


*Fig. 1.* Methods for creating porous materials using spark plasma sintering [35].

The spark plasma sintering method has proven instrumental in producing advanced ceramics such as nanostructural ceramics, functionally graded materials (FGMs), ceramic matrix composites, and nanocomposites. It proves to be an effective, non-conventional sintering method, ensuring the attainment of fully dense materials while preserving nanostructure features [36], [37]. SPS can achieve homogenous, highly dense sintered compacts at faster rates and lower temperatures, resulting in finer microstructures than conventional sintering methods [37]. Besides, SPS can be used to produce compact samples with high porosity (65–80 %), which is higher than using traditional methods (porosity limit – 50 %) for analogical materials [38], [39] and at the same time it is possible to produce corrosion-resistant fibres [40] and demonstrate notably low thermal diffusivity, making them appealing for applications in thermal management [41]. SPS of porous materials is a rapidly advancing field, holding great promise for developing energy-absorption materials, bioimplants, high-temperature filters, fuel cells, and thermoelectric materials [35].

In the current study, we explore the CS compaction and sintering without a matrix to determine behaviour, distinguish the main sintering stages, dependences and characterise material properties. For the first time, this study examines CS compaction behaviour in the SPS process. This study focuses on designing and characterising matrix-less SF foam containing CS only. The influence of sintering temperature, mould diameter (20 and 30 mm diameter), and the size of cenospheres on the properties of sintered

material is investigated. This primary data are essential for designing lightweight and thermally stable (up to 1000 °C) composite materials.

## 2. EXPERIMENTAL

The sintering material used in the study was the CS2 63–150 μm and CS1 150–250 μm fractions produced by burning coal from the Donetsk coal mine. The resulting fly ash of CS1 and CS2 was floated in a mixture of distilled water and ethanol, dried at 105 °C for 12 h, heat treated at 1100 °C for 30 min and fractionated into the above fractions by sieving. In CS1 and CS2, 46 % and 44 % of open volume fractions were observed in the burials of the prepared materials, respectively [8].

The chemical composition (Table 1) of cenospheres is directly related to the inorganic composition of the material burned, as these particles can only be formed from material left over from the combustion process.

**Table 1.** Chemical Composition of Cenospheres [6], [42]–[52]

| | $SiO_2$ | $Al\ O_{23}$ | $Fe\ O_{23}$ | CaO | $K\ O_2$ | MgO | $TiO_2$ | $At\ About_2$ | $P\ O5_2$ | $SO_3$ |
|---|---|---|---|---|---|---|---|---|---|---|
| $W_m$, % | 32.12-64.64 | 13.82-40.7 | 1-14.55 | 0.5-24.49 | 0.4-4.4 | 0.32-3.6 | 0.13-1.79 | 0.02-1.1 | 0.03-0.89 | 0.01-12.03 |

The samples were sintered in SPS sintering machine 'Dr. Sinter SPS825'. The machine is designed for sintering materials at temperatures up to 2400 °C with a sintering force of up to 250 kN. However, in this study, cenospheres were sintered from 1050 °C to 1300 °C at a material sintering force of approximately 0.6 kN using 20 mm, 30 mm, and 50 mm dies. These settings were chosen with the relative brittleness of the material to be sintered, the cenospheres, compared to homogeneous, dense raw materials and the need to produce low-density ceramics.

The samples were prepared for sintering in the SPS machine by lining a 20.7 mm graphite die with 0.35 mm graphite paper, inserting a 20x30 mm bottom plunger and lining its surface in contact with the material to be sintered with 0.35 mm graphite paper, rubbing in 7 grams of 63–150 μm cenospheres, compacting the material to be sintered by gently shaking the die, placing a cylindrical 0.35 mm thick graphite paper on top of the sample to be sintered and inserting the upper graphite plunger into the die. The outside of the die was covered with a 4.5 mm thick carbon fibre thermal insulating material and secured with a carbon fibre cord. The prepared die was placed in the vacuum chamber of the SPS machine with three cylindrical graphite discs of the appropriate size on each side between the plungers of the die and the electrodes of the SPS machine, with 0.35 mm thick graphite paper between the largest of these discs and the electrodes of the machine. The die was placed in a position where the axis of the pyrometer used to measure the temperature coincided with the temperature observation bore so that the temperature was closer to the material to be sintered than to the surface of the die.

The die was inserted into the SPS machine, electrodes adjusted, and clamping force applied (0.6 kN). This pressure, equivalent to 1.9 MPa on a 20 mm die, compressed the sample for 10 minutes. Shrink-

age was measured and held for 20 minutes under reduced atmospheric pressure (6 Pa) until vacuum-related shrinkage ceased. SPS sintering used consistent temperature rise programs, gradually reaching sintering temperature to prevent overheating and sample heterogeneity. Post-sintering, vacuum cooling for 20 minutes ensued until the sample hit around 300 °C. Opening the vacuum chamber accelerated cooling, and 10 minutes later, the sample was extracted. A similar tailored process was applied to samples with diverse cenosphere sizes and die dimensions, adjusting plunger size and material amount accordingly.

## 2.1. Determination of the Quantity of Collapsed Cenospheres

Cenosphere collapse during sample compression and vacuuming in the SPS machine was assessed experimentally. The process involved weighing the material in a mould using an Acculab VIC-612 balance. The material was then placed in a container, covered with deionized water (at least 5 cm thick), mixed, and left to settle for an hour. Floating particles were removed, water was decanted, and the sinking material was transferred to a smaller container. After drying, the mass of collapsed cenospheres was determined.

The apparent density of the sintered samples was determined according to Formula 2.3 using an Acculab VIC-612 balance to determine the weight of the sample.

$$\rho_{\text{apparent}} = \frac{\pi d^2 h}{4m}, \quad (1)$$

where
d – diameter of the sintered sample;
h – height of the sintered sample;
m – mass of the sintered sample.

To assess open porosity, post-sintering materials were sanded to remove graphite paper, dried at 70 °C for four hours, and weighed using an AND GR-200 analytical balance. Boiling in distilled water for four hours saturated open pores. Weight in the water-immersed state was determined using an AD-1653 kit after surface drying. Open porosity, closed porosity, and the ratio of open and closed pore volumes to aluminosilicate volume were calculated. Compressive strength was measured with a Toni Technik ToniNORM model 2020 tester, applying progressively increasing force until a 1.2 % force drop indicated specimen collapse.

XRD analysis employed a Rigaku Ultima+ with a copper cathode X-ray tube (40 kV voltage, 5 mA current). Diffraction images were taken between 5 and 80 ° 2θ at a 4 °/min scan rate. MDI Jade 9 software and electronic ICDD databases PDF-4+ 2023 and PDF-4 Organics were used for phase analysis. Diffraction image preparation in Origin 2023b included noise reduction using an FFT filter with a 5 data point window.

Magnetic fractions of CS 63–150 µm and CS 150–250 µm particles were isolated from the sinterable material. A 30 g layer of the material was spread on paper, and a cylindrical neodymium magnet was moved near the surface. Adhering particles were periodically removed and transferred to a separate container. Fractions were weighed, and the magnetic fraction percentage was calculated using a formula below.

$$W_{mag} = \frac{m_{mag}}{m_{mag}+m_{nonmag}}, \quad (2)$$

where
$mm_{ag}$ – mass of the magnetic fraction of the cenospheres;
$m_{nonmag}$ – mass of the non-magnetic fraction of cenospheres.

## 3. RESULTS AND DISCUSSION

### 3.1. Particle Destruction before the SPS Process

Shrinkage results indicate significant pre-sintering shrinkage in the samples during compression force and vacuum application in the SPS chamber. Approximately 9.7 % and 24.5 % of the initial height of the sample in the die occurred at the time of compression force and vacuum generation, respectively. This initial shrinkage is attributed to cenosphere collapse, validated by the flotation of non-sintered cenospheres in water after force and vacuum application, revealing 21 % and 20 % of collapsed cenospheres, respectively, based on the initial material mass. In a 50 mm die with lower compression force, pressing-induced shrinkage was 0.88 mm, and vacuuming caused no further shrinkage, reducing broken cenospheres to 3 %. The reduced pressure in a larger die likely contributed to this outcome. Testing 150– 250 µm cenospheres in a 20 mm die showed more significant destruction, with 23 % being destroyed after force application and an additional 37 % after vacuuming, surpassing the smaller particle fraction.

### 3.2. Sample Shrinkage during the SPS Process

Figure 2 illustrates that with increasing sintering temperature, the sample height decreases, indicating enhanced particle compaction and softening. This results in reduced open and closed porosity, facilitating more material shrinkage. The data show a trend of reaching a specific shrinkage value at higher temperatures, sharply dropping to zero. This suggests less effective sintering at lower temperatures, with the apparent density approaching that of unsintered particles. Contrary to expectations, attempting to sinter at 1000 °C did not yield cohesive material, as evident in Figs. 3 and 4, where shrinkage started at 900 °C. However, temperature rise reveals a notable difference between measured and sample temperature due to die thermal inertia.

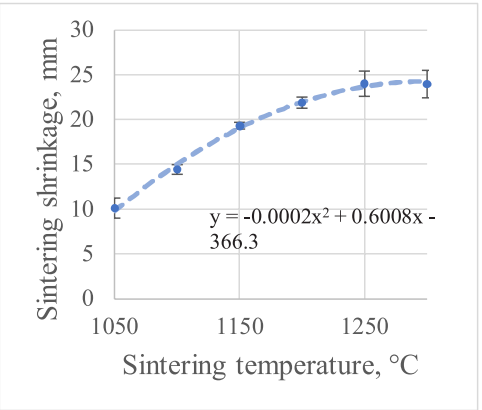


*Fig. 2.* Shrinkage of CS 63–150 µm samples sintered in a 20 mm die during the SPS process as a function of sintering temperature.

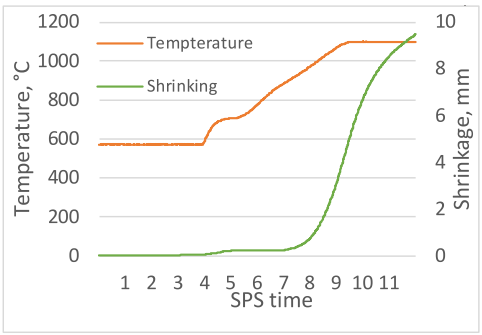


*Fig. 3.* Sintering process data for CS 63–150 µm sample sintered at 1050 °C.

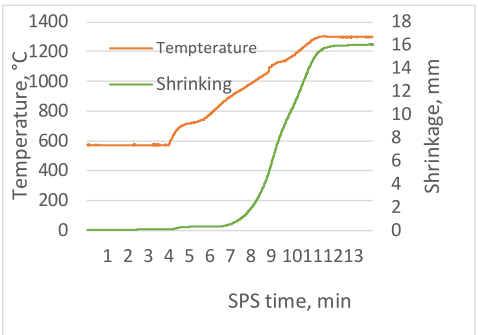


*Fig. 4.* Sintering process data for CS 63–150 µm sample sintered at 1300 °C.

Examining the sintering data in Figs. 3 and 4 reveals that at lower temperatures, the process halts before complete sample shrinkage, indicating incomplete particle sintering. Conversely, at higher temperatures, shrinkage stops shortly after reaching the sintering temperature due to cenosphere softening, expediting equilibrium attainment at the same compression force. Comparing shrinkage at different stages of sample formation exposes peculiarities. Figure 5 indicates that samples from the 150–250 µm cenosphere fraction exhibit less shrinkage during the SPS process, a distinction diminishing with rising sintering temperature. Thicker walls of these particles potentially explain this variance. However, as temperature increases, softening diminishes the impact of thicker walls on mechanical strength. Specimens sintered in 30 mm dies experience reduced shrinkage during pressing and vacuuming due to lower surface pressure from their larger diameter. Yet, their sintering shrinkage is notably higher, likely due to particle breakage or deformation at elevated temperatures, in contrast to samples in 50 mm dies with even lower pressure.

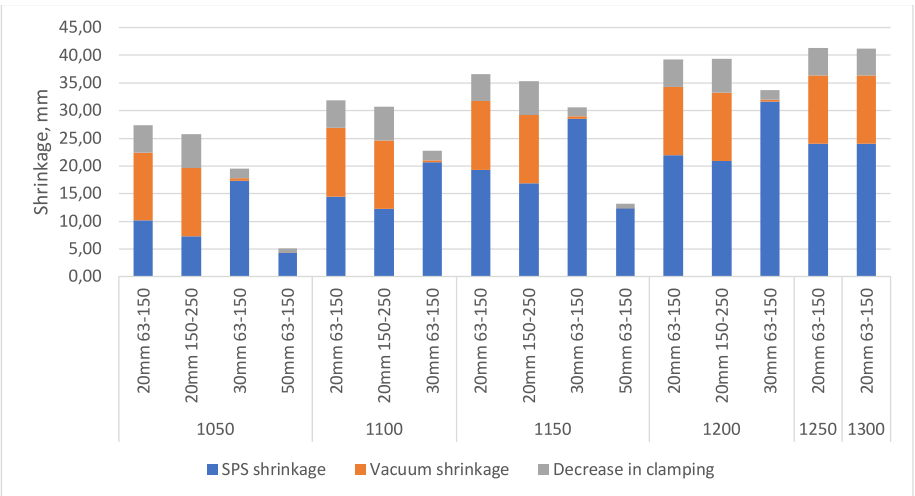


*Fig. 5.* Shrinkage of specimens after squeezing, vacuum and SPS processes, depending on sintering temperature, material used and die diameter.

### 3.3. The Apparent Density of the Resulting Materials

Figure 6 illustrates an increase in the apparent density of sintered cenosphere samples with higher sintering temperatures. However, this relationship is non-linear within the data range. At 1050 °C, complete sintering between particles is inadequate, while at 1300 °C, particles soften and compress. Extending the temperature range for sintering could reveal a trend towards the density of the material in the cenosphere burial at lower temperatures and the proper density of the material forming the cenosphere at higher temperatures. Despite achieving an R2 value of 0.989, a third-order polynomial in non-linear regression analysis may not yield an appropriate function for predicting the data due to these complexities.

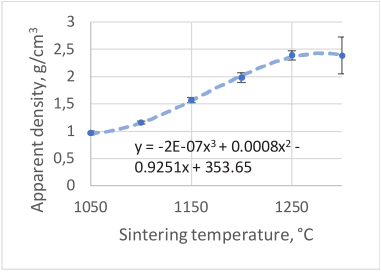


*Fig. 6.* The apparent density of CS 63– 150 µm samples sintered in a 20 mm die as a function of sintering temperature.

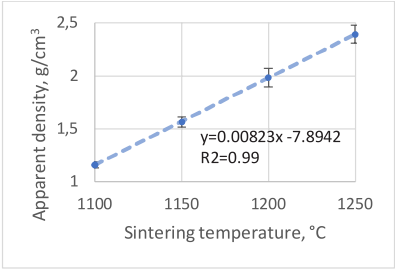


*Fig. 7.* The apparent density of sintered CS 63–150 µm samples versus sintering temperature from 1100 °C to 1250 °C.

In the temperature range of 1100 °C to 1250 °C, a distinct linear increase in density with sintering temperature is evident, depicted in Fig. 7 with R2 = 0.99. The linear regression analysis yields the function ρ=0.0082xT-7.89. This implies that, within these sintering conditions, predicting the apparent density of resulting materials is reliable based on the known sintering temperature.

However, when considering the entire set of samples and individual batches, there is no linear relationship between sample shrinkage and apparent density, contrary to expectations from the apparent density formula. Consequently, estimating this relationship is challenging, but a more feasible approach involves establishing the connection between the measured apparent density and the predicted apparent density derived from observed sample shrinkage.

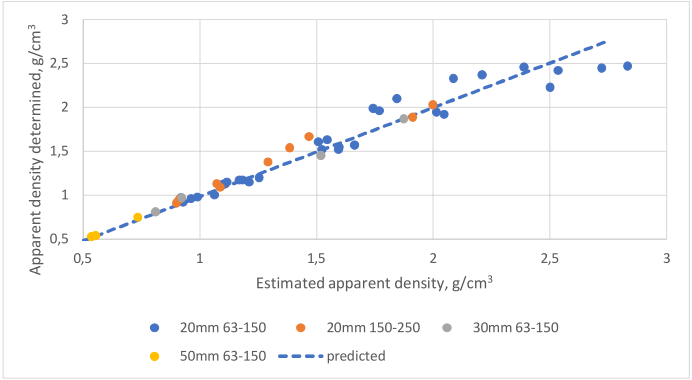


*Fig. 8.* Relationship between predicted and observed apparent density of samples.

Figure 8 reveals an approximately linear relationship between predicted and determined apparent densities. This suggests that knowing the sample shrinkage at all process stages, its initial mass and height, and the internal diameter of the die allows predicting the apparent density of a sintered sample. The data also indicate minimal mass loss during sintering. However, increased scatter in the higher predicted apparent densities results from errors in determining apparent densities, attributed to reduced sample volume and slight material bleed between the die and its plunger at elevated sintering temperatures.

### 3.4. Porosity of the Resulting Materials

The open porosity of the samples, depicted in Fig. 9, diminishes with rising sintering temperature, resulting in samples displaying open porosity ranging from 0.28 % to 43 %. This relationship is nonlinear, with the most pronounced decrease occurring between 1100 °C and 1150 °C. This likely happens because cenosphere particles become soft, allowing for slight deformation and more efficient packing, thereby reducing inter-ionospheric space and closing some open pores. The slowdown in open porosity decrease at higher sintering temperatures is attributed to the increasing difficulty in denser particle packing.

Figure 9 shows that the closed porosity of the sintered materials peaks between 1100 °C and 1200 °C. This is explained by the significant difference in the rate of closed and open pore volume reduction in this temperature range (see Fig. 10). The closed pore volume reduction rate is highest between 1150 °C and 1250 °C, in contrast to 1100 °C and 1150 °C for open pores. This suggests the possibility of producing cenospheric ceramics with a specific open-to-closed pore volume ratio if required.

The total porosity of the sintered samples diminishes with increasing sintering temperature, displaying a strongly linear decrease between 1100 °C and 1250 °C, consistent with the expected trend from apparent density changes with sintering temperature. This alignment supports the reliability of the porosity determination, indicating the absence of gross errors.

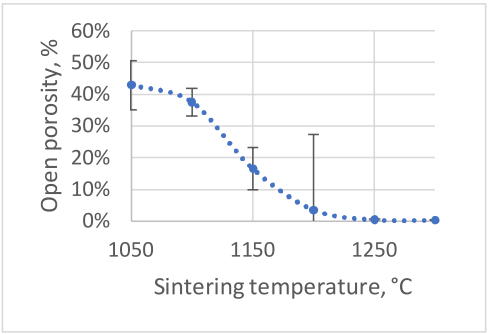


*Fig. 9.* Open porosity of sintered CS 63–150 μm samples as a function of sintering temperature.

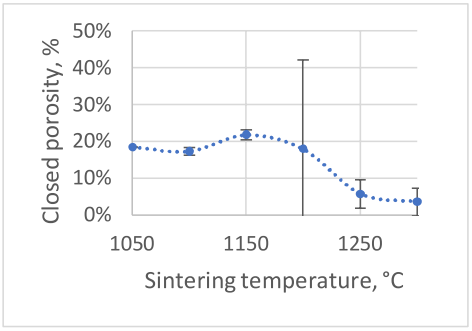


*Fig. 10.* Closed porosity of sintered CS 63–150 μm samples as a function of sintering temperature.

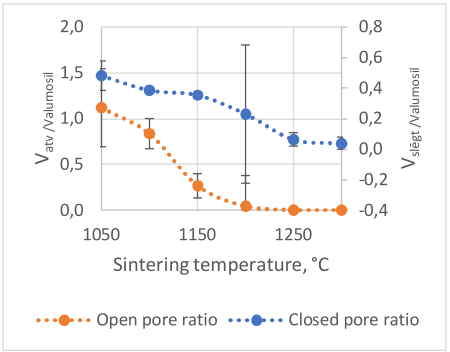


*Fig. 11.* The ratio of closed and open pore volumes of sintered CS 63–150 µm samples to the volume of aluminosilicate as a function of sintering temperature.

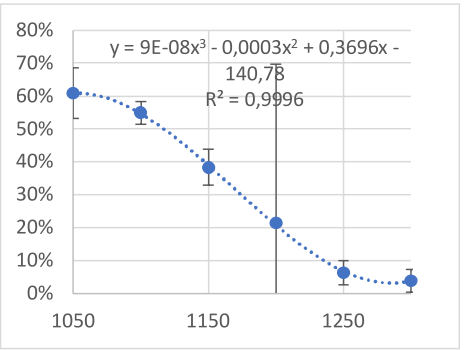


*Fig. 12.* Total porosity of CS 63–150 µm samples sintered in a 20 mm die as a function of sintering temperature.

## 3.5. Morphology of the Resulting Materials

The optical microscopy image in Fig. 13, depicting a CS sample sintered at 1050 °C, reveals that most cenospheres at this temperature remained intact, indicating that the softening point was not reached. Fusion bridges between some cenospheres were observed, but their quantity was visually minimal, contributing to the lower mechanical strength compared to samples sintered at higher temperatures. At this magnification, no notable structural difference was observed between edge and centre regions, suggesting a uniform temperature and compressive force gradient during sintering, similar to sample SPS-944. Some undestroyed cenospheres exhibit translucent bubbles, likely resulting from epoxy partial penetration during sample impregnation, indicating holes in these particles. These holes could stem from cenospheres being too small for water filling during flotation, cracks in walls during pressing or vacuuming, or internal stresses during sample cooling post-sintering.

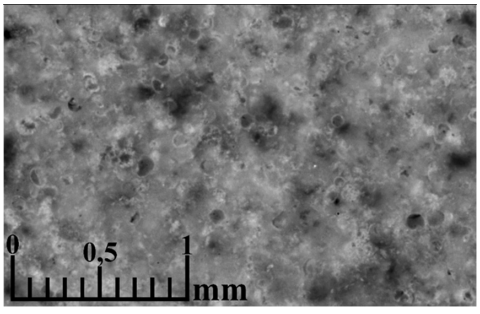


*Fig. 13.* Optical microscopy image of CS 63–150 µm sample SPS-886 sintered at 1050 °C, perpendicular to the squeeze axis.

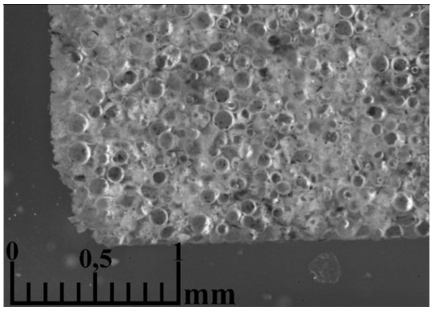


*Fig. 14.* Optical microscopy image of CS 63–150µm sample SPS-944 sintered at 1200 °C, perpendicular to the squeeze axis.

In the sample sintered at 1200 °C (Fig. 14), cenosphere deformation indicates soft melting during sintering, contributing to the formation of compacted regions. Some hollow particles softened enough for the applied compressive force to flatten them, creating

dense material regions. This aligns with the high shrinkage during sintering, increasing with temperature. Magnetic cenospheres, appearing darker in the images, melted and formed higher magnetite content regions in the fused material. Apart from undestroyed cenospheres, numerous plhenospheres are present. Their outer walls melted, but the inner particles largely retained their shape, distinguishing them from the bulk material.

The sample sintered at 1250 °C (Fig. 15) exhibits few closed pores, mainly formed by deformed particles within cenospheres and plhenospheres, resembling the sample sintered at 1200 °C. In Fig. 16, a dense 100 μm thick alloy material layer forms at the die-material interface near the plungers but it is not observed at greater distances. Deeper regions within the material exhibit better sintering, likely due to preferential current flow channels formed during the process. Figure 17 highlights significantly poorer sintering in the sample centre, where the material remains slightly red, indicating potential temperature non-uniformity. This may result from the low electrical and thermal conductivity of the particle, causing outer heating. Addressing this could involve extending the sample curing time for complete heating. However, if incomplete sintering in the sample centre is due to uneven force distribution during SPS, solutions may require increased squeezing force, intensifying shrinkage and apparent density, or a reduction in the h/d ratio, limiting material thickness.

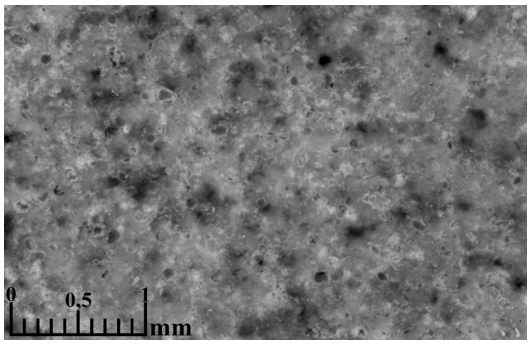


*Fig. 15.* Optical microscopy image of CS 63– 150 μm sample SPS-948 sintered at 1250 °C, perpendicular to the squeeze axis.

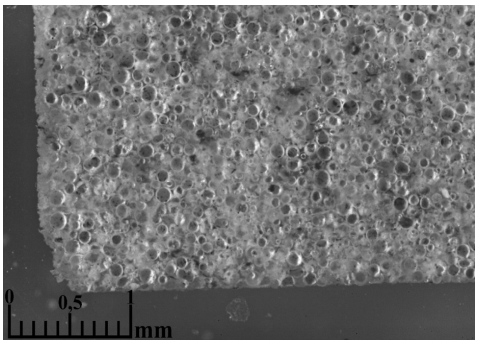


*Fig. 16.* Optical microscopy image of a 50 mm die sintered CS 63–150 μm sample SPS-951 at 1050 °C, parallel to the die axis, close to the material-die boundary.

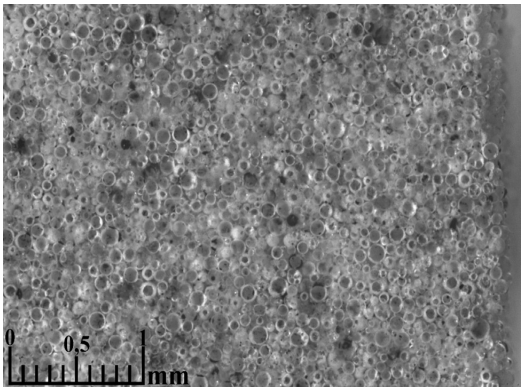


*Fig. 17.* Optical microscopy image of a 50 mm die sintered CS 63–150 μm sample SPS-951 at 1050 °C, parallel to the press axis at the centre of the specimen.

### 3.6. Compressive Strength of the Resulting Materials

All specimens tested exhibit brittleness, which is characterised by spontaneous collapse without significant formation of large cracks or deformation. However, at the highest temperatures, small ceramic pieces detached in some cases due to insufficient sample homogeneity or non-uniform contact surfaces with the testing apparatus. In Fig. 18, compressive strength of the samples increases at higher sintering temperatures. This is likely attributed to enhanced binding between cenospheric particles, particularly noticeable at lower sintering temperatures where particle binding is relatively weak. Additionally, the correlation between density and mechanical strength in high-porosity materials contributes to the observed effect.

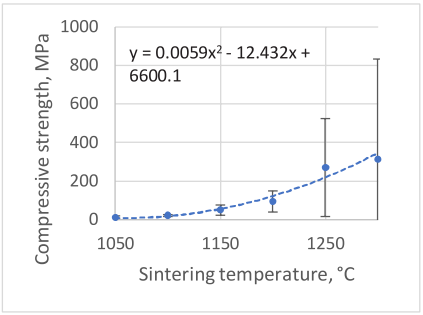


*Fig. 18.* Compressive strength of sintered cenospheric specimens as a function of sintering temperature.

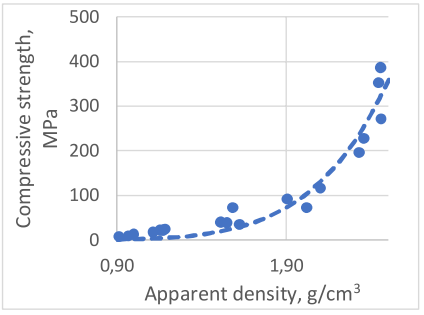


*Fig. 19.* Dependence of compressive strength on apparent density of sintered specimens.

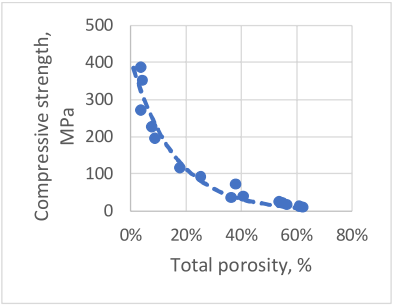


*Fig. 20.* Dependence of compressive strength on total porosity of sintered samples.

The Gibson-Ashby model for predicting the properties of lath-type and porous materials, which is reducible to a power function, does not allow for a conclusive correlation between the compressive strength results obtained for the specimens, giving $R^2$ =0.93. An additional problem is the lack of reliable data on which to base the compressive strength and density of a fully compacted, sintered cenospheric sample. This means that the model cannot be used in this case. The model put forward by Rice gives a visually and mathematically better agreement with $R^2$ =0.94. In addition, this model also gives a reliable value for the compressive strength of a dense material $\sigma_s$ =411.1 MPa since, as mentioned above, these values are not known.

### 3.7. Composition of the Crystalline Phases of the Starting Materials and Samples

Figure 21 indicates no significant phase composition differences between the unsintered material and the sample sintered at 1050 °C. Mullite and an X-ray amorphous phase, likely originating from the amorphous part of the cenospheres predominantly composed of SiO2, are the main components in the range of 18°–27° 2θ. The sample sintered at 1300 °C introduces an additional phase consistent with cristobalite, possibly formed from the partial melting and subsequent crystallization of amorphous cenosphere regions due to slower cooling. Despite confirming the presence of a magnetic phase in some sinterable particles through interaction with an external magnetic field, this crystalline phase is not observed in the XRD results, possibly due to its relatively low content. Weak interaction of the sintered samples with an external magnetic field suggests either retention of some magnetic phase during the SPS process or the generation of another magnetic phase.

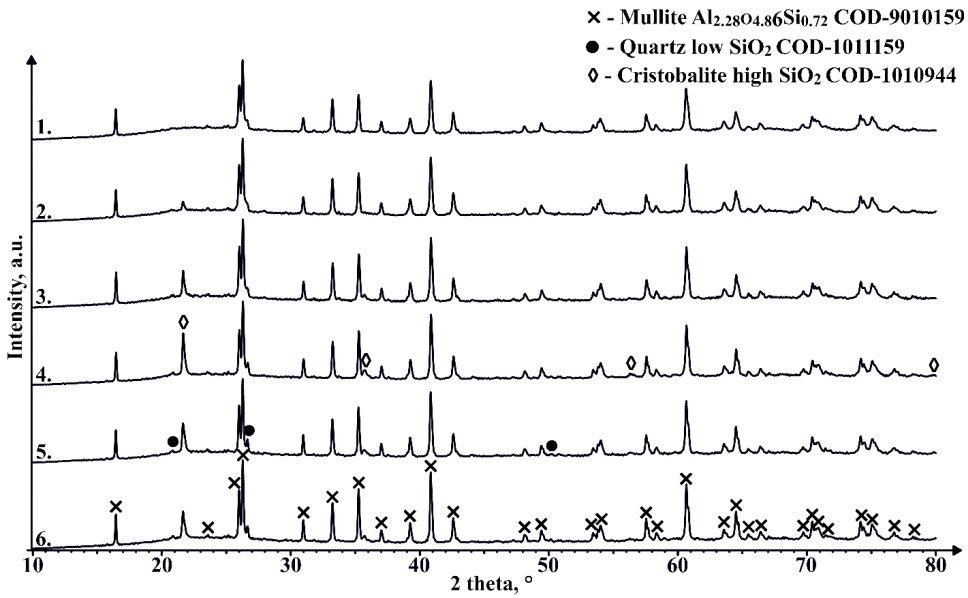


*Fig. 21.* 1050 °C (1), 1100 °C (2), 1150 °C (3), 1200 °C (4), 1250 °C (5) un 1300 °C (6) XRD results of samples sintered in a 20 mm die at 2 min.

## 4. CONCLUSIONS

The sample shrinkage before the beginning of the sintering process decreases with increasing mould diameter, which is caused by decreasing breaking of cenospheres, which can be explained by decreased pressure on the material.

The sample shrinkage during the sintering process began at 900 °C, which shows that using the SPS method, the sintering of cenosphere particles starts between 900 and 1000 °C. Shrinkage of samples during sintering increases with increasing temperature

and decreases with increasing mould diameter.

Increasing sample sintering temperature increases the apparent density of all sample series – CS 63–150μm in 20 mm mould from 0.97 to 2.3 g/cm$^3$ at 1050–1300 °C, in 30 mm mould from 0.81 to 1.87g/cm$^3$ at 1050–1200 °C, in 50 mm mould from 0.54 to 0.75g/cm$^3$ at 1050–1150 °C, while CS 150–250 μm in 20 mm mould from 0.93 to 1.96g/cm$^3$ at 1050– 1200 °C.

Total porosity decreases from 61.5 % to 3.9 %, increasing the sintering temperature from 1050 to 1250 °C, while open porosity starts to decrease at lower temperatures, closed porosity becomes the highest in samples sintered at 1150 °C.

Increasing the sintering temperature from 1050 to 1300 °C, the compressive strength of CS 63–150 samples made in 20 mm mould increases from 11 MPa to 312 MPa. These results correlate with the Rice model, which describes exponential compressive strength dependence on material porosity and completely dense material compressive strength.

The XRD pattern of a sample sintered at 1300 °C temperature reveals a phase not in the unsintered material – cristobalite.

## ACKNOWLEDGEMENTS

The research has been funded by VPP AIPP project No. VPP-AIPP-2021/1-0015 "Combined Lightweight, High-Temperature Resistant Hybrid Composite for Combined Protection of Drones from Direct Energy Weapon". The article has been published with financial support from the Research Support Fund of Riga Technical University.

## REFERENCES

1. Nielsen, L. F. (2005). *Composite Materials*. Springer Berlin Heidelberg. https://doi.org/10.1007/978-3-540-27680-7
2. Qin, Q. H. (2015). Introduction to the composite and its toughening mechanisms. In *Toughening Mechanisms in Composite Materials* (pp. 1–32). Elsevier. https://doi.org/10.1016/B978-1-78242-279-2.00001-9
3. Barbero, E. J. (2010). *Introduction to Composite Materials Design*. CRC Press. https://doi.org/10.1201/9781439894132
4. Shishkin, A., Mironovs, V., Lapkovskis, V., Treijs, J., & Korjakins, A. (2014). Ferromagnetic Sorbents for Collection and Utilization of Oil Products. *Key Engineering Materials*, *604*. https://doi.org/10.4028/www.scientific.net/KEM.604.122
5. Shishkin, A., Mironovs, V., Zemchenkov, V., Antonov, M., & Hussainova, I. (2016). Hybrid Syntactic Foams of Metal-Fly Ash Cenosphere-Clay. *Key Engineering Materials*, *674*. https://doi.org/10.4028/www.scientific.net/KEM.674.35
6. Acar, I., & Atalay, M. U. (2016). Recovery Potentials of Cenospheres from Bituminous Coal Fly Ashes. *Fuel*, *180*, 97–105. https://doi.org/10.1016/j.fuel.2016.04.013
7. Ranjbar, N., & Kuenzel, C. (2017). Cenospheres: A Review. *Fuel*, *207*, 1–12. https://doi.org/10.1016/J.FUEL.2017.06.059
8. Shishkin, A., Abramovskis, V., Zalite, I., Singh, A. K., Mezinskis, G., Popov, V., & Ozolins, J. (2023). Physical, Thermal, and Chemical Properties of Fly Ash Cenospheres Obtained from Different Sources. *Materials*, *16* (5). https://doi.org/10.3390/ma16052035

9. Weise, J., Lehmhus, D., Baumeister, J., Kun, R., Bayoumi, M., & Busse, M. (2014). Production and Properties of 316l Stainless Steel Cellular Materials and Syntactic Foams. *Steel Research International*, *85* (3), 486–497. https://doi.org/10.1002/srin.201300131
10. Yashas Gowda, T. G., Sanjay, M. R., Subrahmanya Bhat, K., Madhu, P., Senthamaraikannan, P., & Yogesha, B. (2018). Polymer Matrix-Natural Fiber Composites: An Overview. *Cogent Engineering*, *5* (1). https://doi.org/10.1080/23311916.2018.1446667
11. Zhang, J., Gong, M., Tian, C., & Wang, C.-A. (2016). Facile Synthesis of Well-Defined CeO2 Hollow Spheres with a Tunable Pore Structure. *Ceramics International*, *42* (5), 6088–6093. https://doi.org/10.1016/j.ceramint.2015.12.166
12. Ozcivici, E., & Singh, R. P. (2005). Fabrication and Characterization of Ceramic Foams Based on Silicon Carbide Matrix and Hollow Alumino-Silicate Spheres. *Journal of the American Ceramic Society*, *88* (12), 3338–3345. https://doi.org/10.1111/j.1551-2916.2005.00612.x
13. Thijs, I., Luyten, J., & Mullens, S. (2003). Producing Ceramic Foams with Hollow Spheres. *Journal of American Ceramic Society, 72* (186975), 2002–2004.
14. Biju-Duval, P. (2007). *A New Porous Material Based on Cenospheres*. Georgia Institute of Technology.
15. Długosz, P., Darłak, P., Purgert, R.M., & Sobczak, J.J. (2011). Synthesis of Light Composites Reinforced with Cenospheres. *Composites, 11* (4), 288–293.
16. Gupta, N. (2007). A Functionally Graded Syntactic Foam Material for High Energy Absorption under Compression. *Materials Letters*, *61* (4–5), 979–982. https://doi.org/10.1016/j.matlet.2006.06.033
17. Gupta, N. (2006). Hollow Particle Filled Composites. *TMS Annual Meeting*, *2006*, 3–13. http://www.scopus.com/inward/record.url?eid=2-s2.0-33646503473&partnerID=tZOtx3y1
18. Lin, T. C., Gupta, N., & Talalayev, A. (2008). Thermoanalytical Characterization of Epoxy Matrix-Glass Microballoon Syntactic Foams. *Journal of Materials Science*, *44* (6), 1520–1527. https://doi.org/10.1007/s10853-008-3074-3
19. Shao, Y., Jia, D., & Liu, B. (2009). Characterization of Porous Silicon Nitride Ceramics by Pressureless Sintering Using Fly Ash Cenosphere as a Pore-Forming Agent. *Journal of the European Ceramic Society*, *29* (8), 1529–1534. https://doi.org/10.1016/j.jeurceramsoc.2008.09.012
20. Wang, C., Liu, J., Du, H., & Guo, A. (2012). Effect of Fly Ash Cenospheres on the Microstructure and Properties of Silica-Based Composites. *Ceramics International*, *38* (5), 4395–4400. https://doi.org/10.1016/j.ceramint.2012.01.044
21. Ren, S., Tao, X., Ma, X., Liu, J., Du, H., Guo, A., … & Ge, J. (2018). Fabrication of Fly Ash Cenospheres-Hollow Glass Microspheres/Borosilicate Glass Composites for High Temperature Application. *Ceramics International*, *44* (1), 1147–1155. https://doi.org/10.1016/j.ceramint.2017.10.089
22. Ren, S., Tao, X., Xu, X., Guo, A., Liu, J., Fan, J., … & Liang, J. (2018). Preparation and Characteristic of the Fly Ash Cenospheres/Mullite Composite for High-Temperature Application. *Fuel*, *233*, 336–345. https://doi.org/10.1016/j.fuel.2018.06.058
23. Sankaranarayanan, S., Nguyen, Q. B., Shabadi, R., Almajid, A. H., & Gupta, M. (2016). Powder Metallurgy Hollow Fly Ash Cenospheres' Particles Reinforced Magnesium Composites. *Powder Metallurgy*, *59* (3), 188–196. https://doi.org/10.1080/00325899.2016.1139339
24. Luong, D., Lehmhus, D., Gupta, N., Weise, J., & Bayoumi, M. (2016). Structure and Compressive Properties of Invar-Cenosphere Syntactic Foams. *Materials*, *9* (2), 115. https://doi.org/10.3390/ma9020115
25. Weise, J., Lehmhus, D., Baumeister, J., Kun, R., Bayoumi, M., & Busse, M. (2014). Production and Properties of 316L Stainless Steel Cellular Materials and Syntactic Foams. *Steel Research International*, *85* (3), 486–497. https://doi.org/10.1002/srin.201300131

26. Rugele, K., Lehmhus, D., Hussainova, I., Peculevica, J., Lisnanskis, M., & Shishkin, A. (2017). Effect of Fly-Ash Cenospheres on Properties of Clay-Ceramic Syntactic Foams. *Materials*, *10* (7). https://doi.org/10.3390/ma10070828

27. Wang, M.-R., Jia, D.-C., He, P.-G., & Zhou, Y. (2011). Microstructural and Mechanical Characterization of Fly Ash Cenosphere/Metakaolin-Based Geopolymeric Composites. *Ceramics International*, *37* (5), 1661–1666. https://doi.org/10.1016/j.ceramint.2011.02.010

28. Baronins, J., Setina, J., Sahmenko, G., Lagzdina, S., & Shishkin, A. (2015). Pore Distribution and Water Uptake in a Cenosphere-Cement Paste Composite Material. *IOP Conference Series: Materials Science and Engineering*, *96* (1), 012011. https://doi.org/10.1088/1757-899X/96/1/012011

29. Adesina, A. (2020). Sustainable Application of Cenospheres in Cementitious Materials – Overview of Performance. *Developments in the Built Environment*, *4*, 100029. https://doi.org/10.1016/j.dibe.2020.100029

30. Shishkin, A., Mironov, V., Zemchenkov, V., Antonov, M., & Hussainova, I. (2016). Hybrid Syntactic Foams of Metal – Fly Ash Cenosphere – Clay. *Key Engineering Materials*, *674*, 35–40. https://doi.org/10.4028/www.scientific.net/KEM.674.35

31. Tatarinov, A., Shishkin, A., & Mironovs, V. (2019). Correlation between Ultrasound Velocity, Density and Strength in Metal-Ceramic Composites with Added Hollow Spheres. *IOP Conference Series: Materials Science and Engineering*, *660* (1). https://doi.org/10.1088/1757-899X/660/1/012040

32. Irtiseva, K., Lapkovskis, V., Mironovs, V., Ozolins, J., Thakur, V. K., Goel, G., … & Shishkin, A. (2021). Towards Next-Generation Sustainable Composites Made of Recycled Rubber, Cenospheres, and Biobinder. *Polymers*, *13* (4), 574. https://doi.org/10.3390/polym13040574

33. Shishkin, A., Drozdova, M., Kozlov, V., Hussainova, I., & Lehmhus, D. (2017). Vibration-Assisted Sputter Coating of Cenospheres: A New Approach for Realizing Cu-Based Metal Matrix Syntactic Foams. *Metals*, *7* (1), 16. https://doi.org/10.3390/met7010016

34. Shishkin, A., Drozdova, M., Kozlov, V., Hussainova, I., & Lehmhus, D. (2017). Vibration-Assisted Sputter Coating of Cenospheres: A New Approach for Realizing Cu-Based Metal Matrix Syntactic Foams. *Metals*, *7* (1). https://doi.org/10.3390/met7010016

35. Dudina, D. V., Bokhonov, B. B., & Olevsky, E. A. (2019). Fabrication of Porous Materials by Spark Plasma Sintering: A Review. *Materials*, *12* (3). MDPI AG. https://doi.org/10.3390/ma12030541

36. Saheb, N., Iqbal, Z., Khalil, A., Hakeem, A. S., Al Aqeeli, N., Laoui, T., … & Kirchner, R. (2012). Spark Plasma Sintering of Metals and Metal Matrix Nanocomposites: A Review. *Journal of Nanomaterials*. https://doi.org/10.1155/2012/983470

37. Tokita, M. (2021). Progress of Spark Plasma Sintering (SPS) Method, Systems, Ceramics Applications and Industrialization. *Ceramics*, *4* (2). https://doi.org/10.3390/ceramics4020014

38. Weise, J., Lehmhus, D., Baumeister, J., Kun, R., Bayoumi, M., & Busse, M. (2014). Production and Properties of 316l Stainless Steel Cellular Materials and Syntactic Foams. *Steel Research International*, *85* (3). https://doi.org/10.1002/srin.201300131

39. Peroni, L., Scapin, M., Lehmhus, D., Baumeister, J., Busse, M., Avalle, M., & Weise, J. (2017). High Strain Rate Tensile and Compressive Testing and Performance of Mesoporous Invar (FeNi36) Matrix Syntactic Foams Produced by Feedstock Extrusion. *Advanced Engineering Materials*, *19* (11). https://doi.org/10.1002/adem.201600474

40. Klymenko, V. M. (2019). Spark Plasma Sintering of Porous Materials Made of 1Kh18N9T Corrosion-Resistant Steel Fibers. *Powder Metallurgy and Metal Ceramics*, *58* (1–2), 23–28. https://doi.org/10.1007/s11106-019-00043-6

41. Manukyan, K. V., Yeghishyan, A. V., Shuck, C. E., Moskovskikh, D. O., Rouvimov, S., Wolf, E. E., & Mukasyan, A. S. (2018). Mesoporous Metal - Silica Materials: Synthesis, Catalytic and Thermal Properties. *Microporous and Mesoporous Materials*, *257*. https://doi.org/10.1016/j.micromeso.2017.08.044
42. Vassilev, S. V., Menendez, R., Diaz-Somoano, M., & Martinez-Tarazona, M. R. (2004). Phase-Mineral and Chemical Composition of Coal Fly Ashes as a Basis for their Multicomponent Utilization. 2. Characterization of Ceramic Cenosphere and Salt Concentrates. *Fuel*, *83* (4–5), 585–603. https://doi.org/10.1016/J.FUEL.2003.10.003
43. Jung, J., Kim, S. H., Kang, J. H., Park, J., Kim, W. K., Lim, C. Y., & Park, Y. H. (2022). Compressive Strength Modeling and Validation of Cenosphere-Reinforced Aluminum–Magnesium-Matrix-Based Syntactic Foams. *Materials Science and Engineering A*, *849*. https://doi.org/10.1016/j.msea.2022.143452
44. Yu, J., Li, X., Fleming, D., Meng, Z., Wang, D., & Tahmasebi, A. (2012). Analysis on Characteristics of Fly Ash from Coal Fired Power Stations. *Energy Procedia*, *17*, 3–9. https://doi.org/10.1016/j.egypro.2012.02.054
45. Yoriya, S., Intana, T., & Tepsri, P. (2019). Separation of Cenospheres from Lignite Fly Ash Using Acetone-Water Mixture. *Applied Sciences (Switzerland)*, *9* (18). https://doi.org/10.3390/app9183792
46. Jiang, F., Zhang, L., Mukiza, E., Qi, Z., & Cang, D. (2018). Formation Mechanism of High Apparent Porosity Ceramics Prepared from Fly Ash Cenosphere. *Journal of Alloys and Compounds*, *749*, 750–757. https://doi.org/10.1016/j.jallcom.2018.03.303
47. Rugele, K., Lehmhus, D., Hussainova, I., Peculevica, J., Lisnanskis, M., & Shishkin, A. (2017). Effect of Fly-Ash Cenospheres on Properties of Clay-Ceramic Syntactic Foams. *Materials*, *10* (7). https://doi.org/10.3390/ma10070828
48. Nithyanandam, A., & Deivarajan, T. (2021). Development of Fly Ash Cenosphere-Based Composite for Thermal Insulation Application. *International Journal of Applied Ceramic Technology*, *18* (5), 1825–1831. https://doi.org/10.1111/ijac.13767
49. Kristombu Baduge, S., Mendis, P., San Nicolas, R., Nguyen, K., & Hajimohammadi, A. (2019). Performance of Lightweight Hemp Concrete with Alkali-Activated Cenosphere Binders Exposed to Elevated Temperature. *Construction and Building Materials*, *224*, 158–172. https://doi.org/10.1016/j.conbuildmat.2019.07.069
50. Kolay, P. K., & Singh, D. N. (2001). Physical, Chemical, Mineralogical, and Thermal Properties of Cenospheres from an Ash Lagoon. *Cement and Concrete Research, 31*, 539– 542.
51. Anshits, N. N., Mikhailova, O. A., Salanov, A. N., & Anshits, A. G. (2010). Chemical Composition and Structure of the Shell of Fly Ash Non-Perforated Cenospheres Produced from the Combustion of the Kuznetsk Coal (Russia). *Fuel*, *89* (8), 1849–1862. https://doi.org/10.1016/j.fuel.2010.03.049
52. Patel, S. K., Majhi, R. K., Satpathy, H. P., & Nayak, A. N. (2019). Durability and Microstructural Properties of Lightweight Concrete Manufactured with Fly Ash Cenosphere and Sintered Fly Ash Aggregate. *Construction and Building Materials*, *226*, 579–590. https://doi.org/10.1016/j.conbuildmat.2019.07.304